

SANDIA REPORT

SAND2010-7284

Unlimited Release

Printed October 2010

MEASUREMENTS OF PROMPT RADIATION INDUCED CONDUCTIVITY OF KAPTON

E. F. Hartman, T. A. Zarick, T. J. Sheridan, E. F. Preston and T. A. Stringer

Prepared by
Sandia National Laboratories
Albuquerque, New Mexico 87185 and Livermore, California 94550

Sandia National Laboratories is a multi-program laboratory managed and operated by Sandia Corporation, a wholly owned subsidiary of Lockheed Martin Corporation, for the U.S. Department of Energy's National Nuclear Security Administration under contract DE-AC04-94AL85000.

Approved for public release; further dissemination unlimited.

Issued by Sandia National Laboratories, operated for the United States Department of Energy by Sandia Corporation.

NOTICE: This report was prepared as an account of work sponsored by an agency of the United States Government. Neither the United States Government, nor any agency thereof, nor any of their employees, nor any of their contractors, subcontractors, or their employees, make any warranty, express or implied, or assume any legal liability or responsibility for the accuracy, completeness, or usefulness of any information, apparatus, product, or process disclosed, or represent that its use would not infringe privately owned rights. Reference herein to any specific commercial product, process, or service by trade name, trademark, manufacturer, or otherwise, does not necessarily constitute or imply its endorsement, recommendation, or favoring by the United States Government, any agency thereof, or any of their contractors or subcontractors. The views and opinions expressed herein do not necessarily state or reflect those of the United States Government, any agency thereof, or any of their contractors.

Printed in the United States of America. This report has been reproduced directly from the best available copy.

Available to DOE and DOE contractors from

U.S. Department of Energy
Office of Scientific and Technical Information
P.O. Box 62
Oak Ridge, TN 37831

Telephone: (865) 576-8401
Facsimile: (865) 576-5728
E-Mail: reports@adonis.osti.gov
Online ordering: <http://www.osti.gov/bridge>

Available to the public from

U.S. Department of Commerce
National Technical Information Service
5285 Port Royal Rd.
Springfield, VA 22161

Telephone: (800) 553-6847
Facsimile: (703) 605-6900
E-Mail: orders@ntis.fedworld.gov
Online order: <http://www.ntis.gov/help/ordermethods.asp?loc=7-4-0#online>



SAND2010-7284
Unlimited Release
Printed October 2010

MEASUREMENTS OF PROMPT RADIATION INDUCED CONDUCTIVITY OF KAPTON

E. F. Hartman, T. A. Zarick and T.J. Sheridan, Department, 01343

Sandia National Laboratories
P. O. Box 5800
Albuquerque, New Mexico 87185-MS 1167

E. F. Preston and T. A. Stringer
ITT Corporation
5009 Centennial Blvd.
Colorado Springs, CO 80919

Abstract

We performed measurements of the prompt radiation induced conductivity in thin samples of Kapton (polyimide) at the Little Mountain Medusa LINAC facility in Ogden, UT. Three mil samples were irradiated with a 0.5 μ s pulse of 20 MeV electrons, yielding dose rates of 1E9 to 1E10 rad/s. We applied variable potentials up to 2 kV across the samples and measured the prompt conduction current. Analysis rendered prompt conductivity coefficients between 6E-17 and 2E-16 mhos/m per rad/s, depending on the dose rate and the pulse width.

ACKNOWLEDGEMENTS

The authors acknowledge the support provided by Boeing personnel at the Little Mountain Test Facility (LMTF), Hill AFB, Ogden, Utah. The editing of this report was performed by Diana Wrobel. Funding for this work was to a great extent provided by the Radiation Effects Sciences Program Area.

Table of Contents

1. Introduction.....	7
2. Experimental Apparatus.....	8
Electron Beam Characteristics.....	11
3. Procedures.....	13
Dosimetry.....	15
Environment at the Test Fixture	17
4. Analysis.....	17
Dose Rates	19
Energy Deposition	19
Charge Deposition	21
5. Results.....	22
Data Reduction.....	23
Direct drive measurements	24
Biased Response	27
Determining the RIC coefficient.....	32
Summary	33
Comparisons	36
Bibliography	38
Distribution	40

Table of Figures

Figure 1 A RIC cell test fixture.....	8
Figure 2 A typical RIC cell.....	3
Figure 3 The vacuum experimental chamber shown in the foreground	10
Figure 4 The experiment chamber with high voltage cables.....	10
Figure 5 The LINAC electron energy spectrum.	3
Figure 6 Some typical electron pulse time waveforms.....	3
Figure 7 Electron energy spectra measured at different pulse widths.....	13
Figure 8 The dose ratio between the TLD and silicon calorimeter.....	15
Figure 9 Comparison of dosimeter methods.....	16
Figure 10 Equivalent Electrical Measurement Circuit.....	3
Figure 11 The differential dose profile computed by Adept.....	3
Figure 12 Electron energy spectra from MCNP.	3
Figure 13 Shot 1197 data, raw and with a 65 point Savitzky-Golay filter applied.....	3
Figure 14 Raw and filtered data from shot 1188 (series K3b).....	3

Figure 15 Typical zero bias waveforms..... 3

Figure 16 Zero bias shots from series K3b. 3

Figure 17 Peak measured voltage of zero bias shots vs. dose rate, with linear fits. 3

Figure 18 PCD and RIC signals for Shot 2021 of series K3a..... 3

Figure 19 Shot 2440 from Series 3c. 3

Figure 20 Shots from Series 5..... 3

Figure 21 Comparison of RIC Coefficient fit for different methods of determining the peak voltage. 3

Figure 22 Determining the RIC coefficient for K2 URC using the average dose rate. 3

Figure 23 Determining the RIC coefficient of K2 URC using individual dose rates. 3

Figure 24 Summary of Measured RIC Coefficients. 3

Figure 25 Summary of Conductivity Measurements with Fit 3

Figure 26 Comparisons of Conductivity with Previous Results..... 3

1. Introduction

Kapton[®], a polyimide film developed by DuPont¹, is commonly used in military systems and other space systems which can be exposed to high ionizing dose rates. Ionizing radiation can render a dielectric material conducting by producing electron-hole pairs in the material [1] [2] [3] [4]. The electrons and holes are quickly trapped, but possess some mobility during their lifetime and increase the conductivity of the dielectric. An increase of conductivity that persists only during the radiation pulse is called the *prompt conductivity*. There may also be a *delayed conductivity* that decays slowly after exposure to radiation.

Kapton is a highly insulating organic polymer with low mobility. It is likely that radiation-induced carrier generation and recombination are diffusion-controlled processes with the effective cross-sectional radius of traps being larger than the carrier mean free path.

There is no successful analytic model of radiation-induced conductivity (RIC) in dielectrics, as the processes determining the lifetime and mobility electrons and holes are numerous and complex. In polymers, fundamental differences in bonding, morphology, and structure lead to entirely different mechanisms for the transport of electrons [5]. We must rely on experiments to determine the conductivity of a material as a function of dose rate. This report compiles RIC data on thin Kapton samples that were done at the Little Mountain Medusa LINAC facility between May 2005 and December 2008.

¹ DuPont[™] and Kapton[®] are trademarks or registered trademarks of E.I. du Pont de Nemours and Company.

2. Experimental Apparatus

Figure 1 shows a side view cross-section of the RIC test fixture for the dielectric samples. This configuration is a stack of two separate cells which are irradiated together. Each cell consists of a center electrode, two dielectric layers, and ground planes on the outer surface of each dielectric. The RIC cell nearest the electron beam is called the upper RIC cell (URC), and the cell below it the lower RIC cell (LRC).

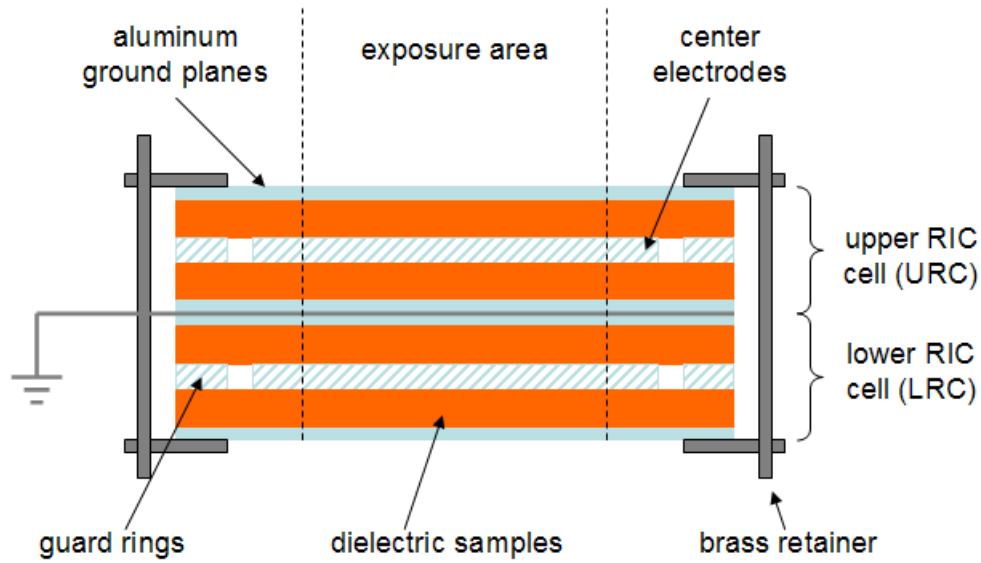


Figure 1 A RIC cell test fixture.

The Kapton layers are formed from 76.2 micron thick discs, about 2.5 centimeters in diameter, and are placed on either side of a 30 micron center aluminum electrode. Two 15 micron outer aluminum electrodes serve as the cell ground planes. The guard rings minimize the electric field distortion at the edge of the center electrodes. Bias voltages were applied to the center electrodes and the guard rings. The bias of the lower cell was made equal to that of the upper cell, with opposite polarity.

Current is driven through the dielectric layers from their conductivity and the applied bias, and directly from the attenuation and divergence of the electron beam. The conductivity consists of the dark or static conductivity σ_0 , the prompt RIC σ_p , and the delayed RIC σ_d . The net current is the sum

$$I = Vd(\sigma_0 + \sigma_p + \sigma_d) + I_{dd} \quad (1)$$

where V is the bias, and d the sample thickness. The delayed conductivity may contain several terms with different decay constants, representing traps of different depths. In

addition, there is a direct drive current I_{dd} produced by the electron beam in the absence of bias.

This cell design, including dielectric layers above and below a center electrode, greatly reduces the direct drive current, I_{dd} by balancing the charge lost from the center electrode on either side. Even with this technique, the direct drive current is a substantial part of the total, and it can be difficult to determine the contribution of the prompt RIC.

A typical RIC cell test fixture is pictured in Figure 2. The busses for applying the guard ring voltages (LGR and UGR) and the center electrode biases (URC and LRC) are labeled.

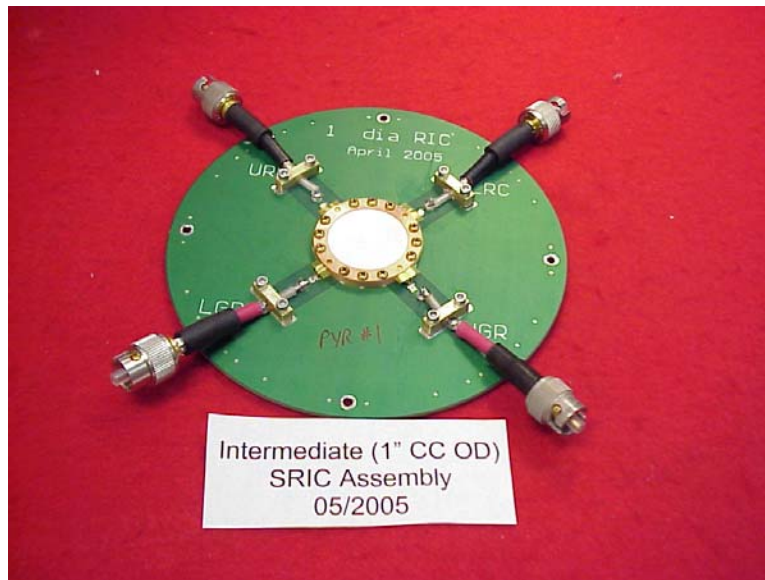


Figure 2 A typical RIC cell.

The properties of the Kapton samples under test are given below.

Composition (weight fractions): H 0.0262, C 0.6911, N 0.0733, O 0.2094

Density: 1.42 g/cc

Dielectric constant: 3.5

Sample thickness: 3.00 mils = 76.2 microns

The measured capacitance of the RIC cells containing kapton is 410 ± 2 pF. This is for one two-sided cell, either the URC or the LRC. The area of the center electrode is $A_{tot} = 5.06 \text{ cm}^2$, but the irradiated area was collimated to 1.98 cm^2 . The measured capacitance agrees with a one-dimensional calculation:

$$C = \frac{2A_{tot}\kappa\epsilon_0}{d} = \frac{2(5.06 \times 10^{-4} \text{ m}^2)(3.5)(8.9 \times 10^{-12} \text{ F / m})}{76.2 \times 10^{-6} \text{ m}} = 410 \text{ pF} . \quad (2)$$

The test chamber that housed the RIC cell was evacuated to $2E-4$ Torr to eliminate any effects due to air ionization. Radiation entered the test chamber through a collimated aperture. Figure 3 shows the front side of the test chamber and the aperture hole in the center of the fixture. The aperture was smaller in diameter than the dielectric samples, assuring that only the central area of the dielectric was struck by radiation, and that the guard rings did not receive radiation exposure.

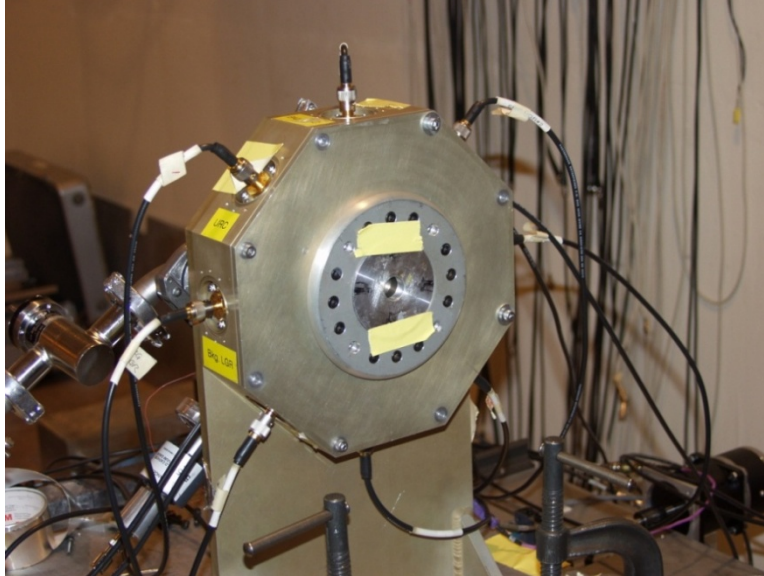


Figure 3 The vacuum experimental chamber shown in the foreground with high voltage cables exiting through vacuum feed-through connectors.

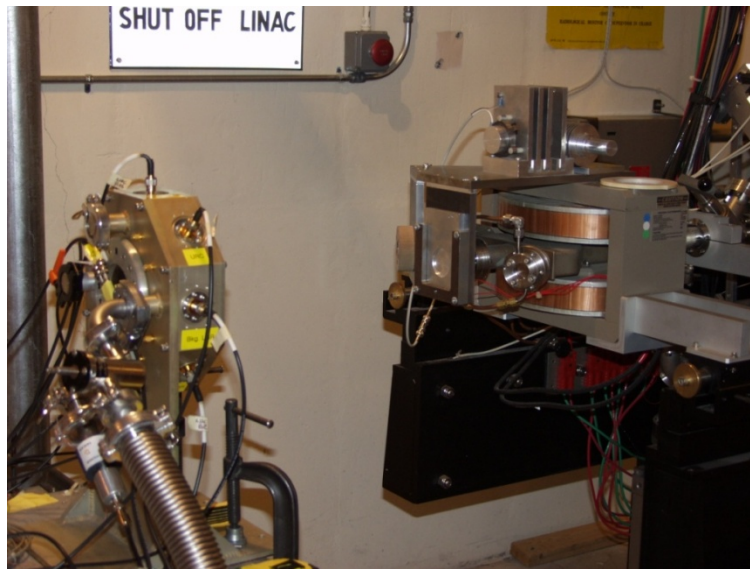


Figure 4 The experiment chamber with high voltage cables. In the background is the front of the Medusa Linear Accelerator at the LMTF at Hill AFB near Ogden Utah.

Electron Beam Characteristics

If a radiation source is not capable of providing consistent or repeatable output, including its spectrum, pulse width, and fluence, then the difficulty of performing repeatable and interpretable experiments is greatly magnified. We chose the Medusa LINAC at the Little Mountain Test Facility (LMTF) because it is capable of producing repeatable and predictable radiation output over long periods of time (such as reproducible pulsing over a week of experiments). We found through repeated testing that our dosimetry consisting of silicon calorimeter, PIN diode and PCD diamond detectors gave consistent repeatable readings shot to shot for the same conditions such as fixed distance from the source and fixed pulse width. The variation at the same conditions was approximately 1% shot to shot.

The nominal electron energy for the LINAC is 20 MeV, and the radiation pulse can be varied from 10 ns to 50 μ s. For most of these experiments the radiation pulse width was about 0.5 μ s FWHM. The dose rate range for this experiment was 1E9 to 1E10 rad(Si)/s. For electron beam dosimetry, silicon calorimeters were supplemented with TLDs, PIN diodes, and PCDs. Measurement accuracy at the LINAC, including dosimetry and recording instruments, is estimated to be about $\pm 10\%$.

The electron beam differential energy spectrum is shown in Figure 5. The average electron kinetic energy for this spectrum is 19.2 MeV.

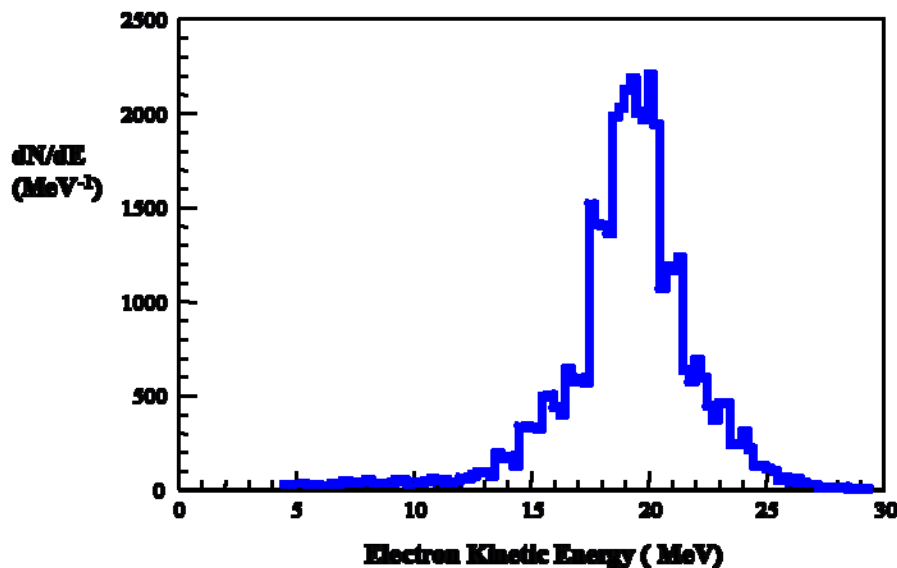
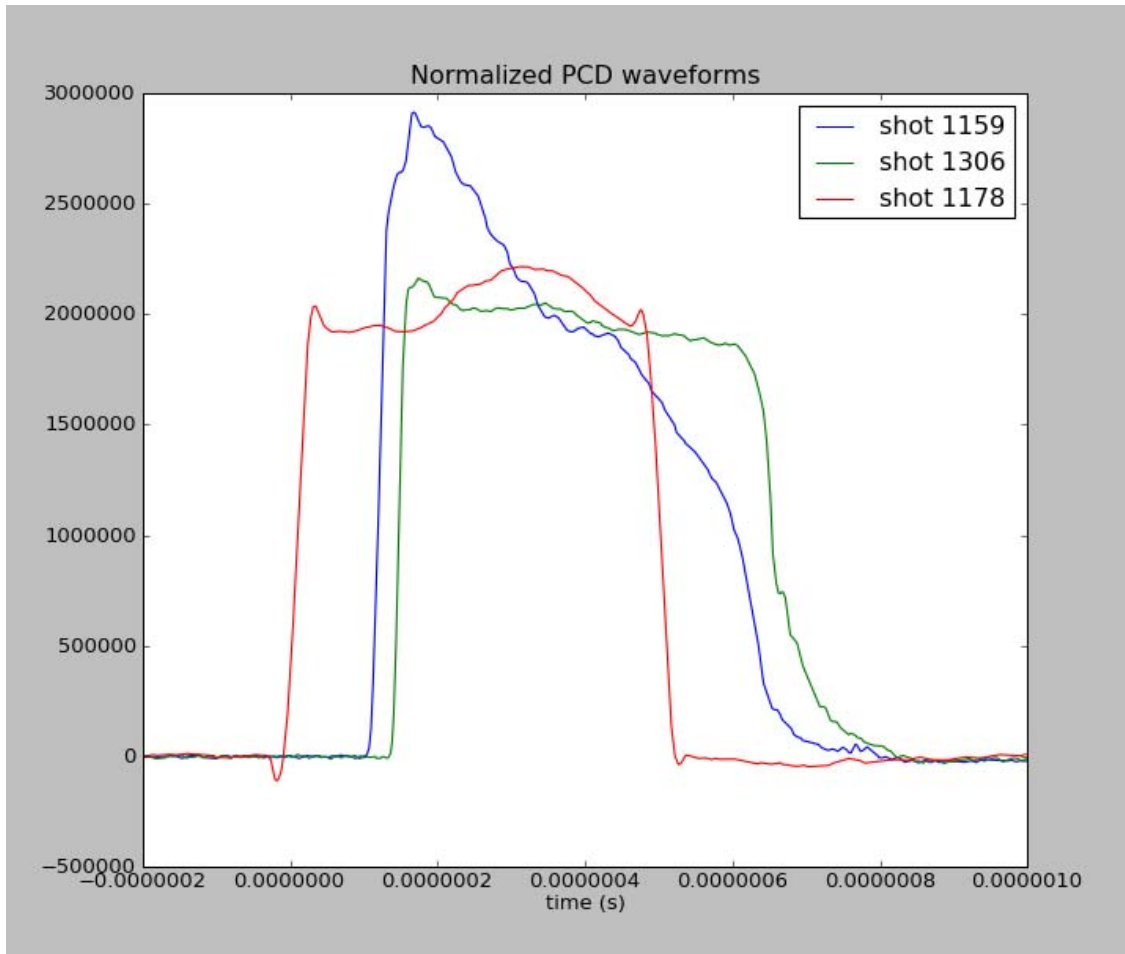


Figure 5 The LINAC electron energy spectrum.

The range of 20 MeV electrons in silicon or Aluminum is about 5 cm, which is much greater than the total thickness of the test fixture (about 0.7 cm), so the dose should be nearly constant in all four Kapton layers.

A few typical radiation waveforms are shown in Figure 6. Most pulses are relatively flat, but some series of shots regularly exhibit peaks in the early or late times.



**Figure 6 Some typical electron pulse time waveforms
(As measured by diamond PCD's).**

The LINAC pulse has a microstructure with many short pulses of 40-80 ps duration at a rate of about 1.3 GHz. We have not found any reports that this microstructure creates any problems for testing when ionizing dose or dose rate drives the response. An extremely fast circuit could respond to the microstructure.

We investigated the LINAC spectrum as the pulse width of the LINAC was changed. A plot of the Medusa LINAC electron energy spectrum is shown in Figure 7 for both 5 and 50 microsecond pulses. The measurement was made by using bending magnets to divert electrons of nearly discrete energy to a 30 degree port. The response was recorded with a Faraday Cup. It can be seen in figure 7 that the electron energy peaks at around 19-20 MeV for both spectra and falls rapidly above 25 and below 10 MeV. The spectrum was measured between 5 and 30 MeV. Given that the spectral shape is nearly identical at 5 and 50 microsecond pulse widths, there are not any significant uncertainties associated with experiments performed at different pulse widths on the LINAC that are caused by spectral variations.

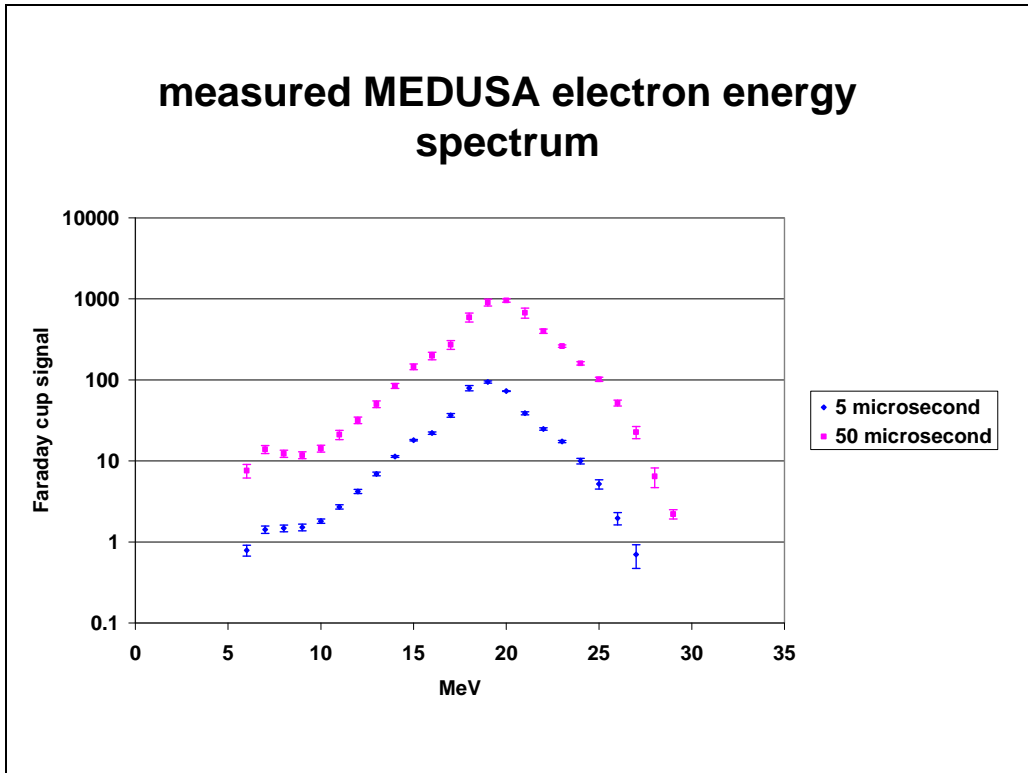


Figure 7 Electron energy spectra measured at different pulse widths.

3. Procedures

We included an aluminum scatter plate of 0.80 cm thickness on the front of the LINAC. We collimate the electron beam so only the dielectric samples are exposed to the beam, assuring that instrumentation cables are not exposed. The diameter of the collimator is tailored to a size such that guard rings are not exposed to direct radiation.

The response of different individual samples of the same type, on the same shot could vary. Though the dielectric samples are fabricated in the same manner there may be slight differences. We are reporting data from four different text fixtures (K1, K2, K3, and K5), each of which has hosts two cells (URC and LRC). The results seem consistent within experimental errors between the different samples.

The radial location for the experiment is established by first assuring our experiment is aligned with the center of the LINAC beam. This is accomplished using the low power alignment laser supplied by the LMTF and mounted on the back wall of the facility. Without our vacuum fixture in place, we burn a spot in a plastic film to establish the center of the LINAC beam. The laser is then aligned to this center position. We then move our vacuum fixture in place and align the laser to the back of our fixture which has cross-hair indicators. The circuit board with dielectric samples aligns to the back cross hairs by being securely bolted in a rigid position within the vacuum chamber.

We established the desired axial position away from the LINAC beam port for each pulse length by mounting the silicon calorimeter in the position where the samples will be during testing. We find the axial position that provides the desired dose (say 10 kilorads) for a particular pulse width.

Next we exposed the dielectric samples at zero bias and record the current through the measurement circuit during the radiation pulse. Then we put bias on the samples and step through a series of exposures at various increasing bias levels (+/-). Typically we recorded several results at each bias level and alternate bias conditions (+ or -) on each dielectric sample.

When polymers are irradiated with photons or electrons, space charge can build up within the material sample. The accumulation of fixed trapped space charge will distort the internal field. The trapped charge effect becomes severe as the field strength approaches that produced by the externally applied bias. Discharge of the trapped charge after each data recording was accomplished by multiple zero bias irradiations until the recorded current signal returned the initial zero bias conditions. Polarities of the applied bias were also reversed at each bias voltage

The radiation is shielded and collimated such that virtually no radiation will strike any coaxial instrumentation or bias cables exiting the test chamber. Also the test board and buried traces are minimized by restricting the area and circuit traces and attachments to that sufficient to mount the dielectric test cells, and to instrument and supply bias to the samples. The Tungsten collimator no doubt produces some Bremsstrahlung radiation at the high electron energies of the LINAC. This radiation strikes some of the traces and cabling. This produces a small source of error because the background measurements are small compared to the measurements on the test samples.

Air can become conductive when ionized by radiation, which might provide a leakage path to discharge the voltage in our RIC samples. Sometimes experimenters coat all metal or conductors under voltage with dielectric materials. While this can often eliminate most leakage induced by radiation it could potentially introduce possible charging effects, particularly in electron beam experiments.

We chose to place our samples in a vacuum chamber to eliminate the possibility of any air ionization effects. We used a chamber large enough in diameter and thin enough such that essentially no collimated scattered or reradiated (Bremsstrahlung) radiation of any

significance could ionize trapped air within cables outside our experiment. We allowed the collimated electron beam to transit our thin front window of 0.00254 cm Titanium and the thin vacuum chamber housing back cover and “get lost” in the LINAC facility room. Our background response was very low compared to our test response.

Dosimetry

We used Si calorimeters as our base dose diagnostic. Si calorimetry is recommended rather than the thermoluminescent dosimetry (CaF₂ TLDs) frequently used in radiation testing. Experiments show that the CaF₂ TLD and calorimetry readings diverge at high doses. An example of divergence is shown in figure 8. CaF₂ TLD response is complex and is subject to general sources of systematic error, including trap saturation, space charge effects in e-beam testing etc. Therefore, Si calorimeter techniques are recommended over CaF₂ TLDs. The overall RMS error associated with our Si calorimeter was 7%. This error included the amplifier, Yokogawa DL750 digitizer, the thermocouple hardware and reading technique.

Simultaneous calorimetry measurements at the various intended sample locations were taken to establish systematic ratios in the expected dose where possible. Calculations show that for 20 Mev electrons, the dose into 0.10 cm of Si is 1.31 Mev-cm²/g and the dose into 0.089 cm of CaF₂ is 1.33 Mev-cm²/g. The calculated values are essentially identical for deposited dose in realistic thicknesses of both the Si calorimeter and the CaF₂ TLD.

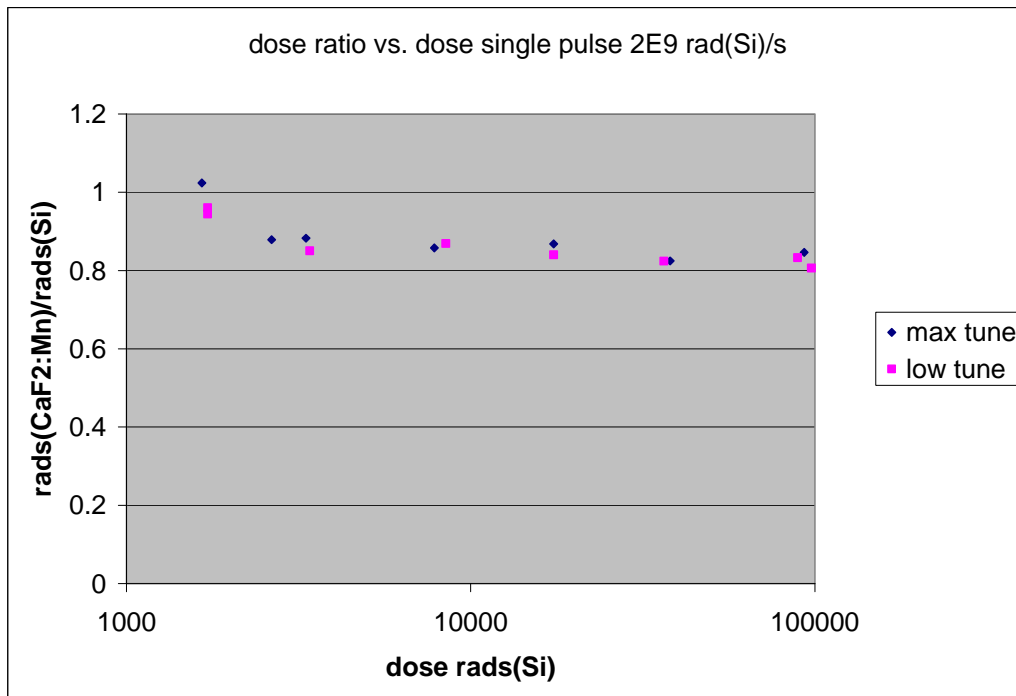


Figure 8 The dose ratio between the TLD and silicon calorimeter.

Lithium Fluoride (LiF) TLDs are also sometimes used as dosimeters in radiation effects testing, but are known to have problems at high dose and high dose rates. In one study

we performed on LINAC dosimetry techniques we found the LiF measurements to be problematic and unreliable.

Figure 9 presents a comparison of several diagnostic methods. The methods include PIN diodes, Faraday cup, neutron-damaged transistor, diamond detectors (PCDs), silicon calorimeter and LiF thermoluminescent detectors (TLDs).

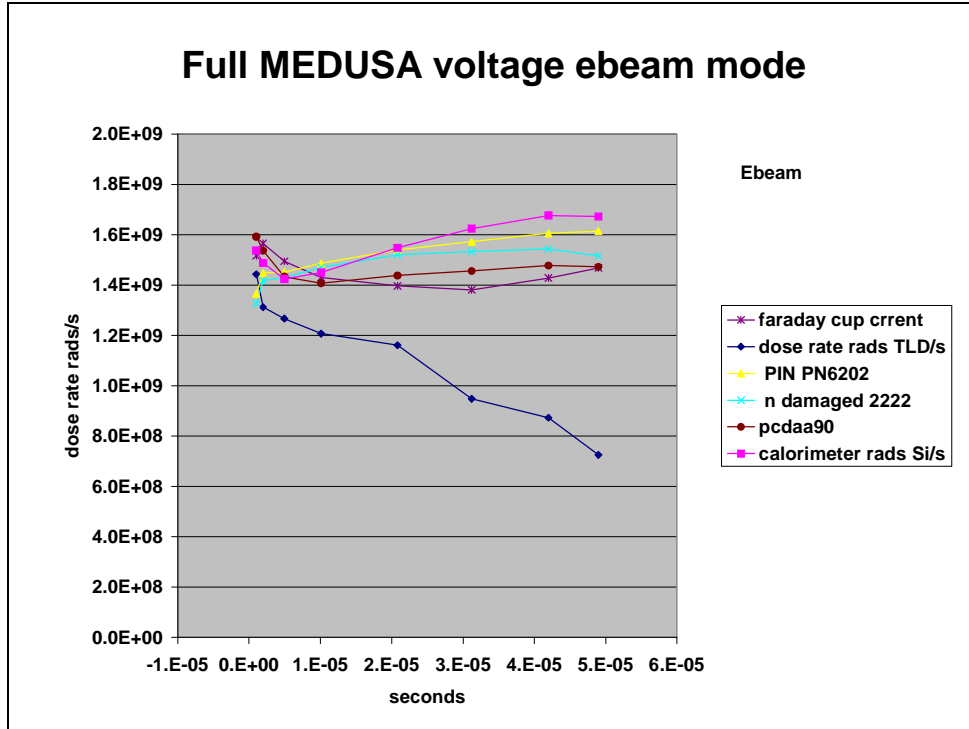


Figure 9 Comparison of dosimeter methods.

The shapes of the diagnostics generally agree, with the exception of the TLDs. Some differences are expected because of geometry and material differences between the various diagnostics. PIN diodes, the damaged transistors, and the silicon calorimeter are all silicon based diagnostics, and they track each other well (top three curves). The Faraday cup response is just below the silicon diagnostics, and is a measure of beam current not affected by material cross sections. The PCD is a carbon based material and its spectral response is probably slightly different than the silicon-based diagnostics. The LiF response is an outlier.

It is likely that LiF and perhaps even CaF_2 can have problems if there are too many carriers generated and there are not enough traps present. The sensitivity and dose measuring ability of TLDs will change when the number of carriers becomes a significant fraction of the traps. Lifetimes, trapping efficiencies and other factors will determine how well a dosimeter performs. The dosimeter can be stressed at high dose rates or lower dose rates for longer times as long as the radiation pulses are shorter than the lifetimes of the processes occurring. This under-reading behavior can be considered a saturation effect. We use the silicon dosimeter as our base diagnostic. Based on the data we trust this technique accurately records dose (Si) to within 7% accuracy. We further

correct our silicon calorimeter shot to shot for the small (1-2%) source output variation of the LINAC using calibrated PIN diodes and PCDs in fixed positions just behind our test dielectric samples

Environment at the Test Fixture

Since we do not simultaneously measure the dose with the silicon calorimeter and expose the test samples, we must assure ourselves we know the environment at the samples. One fact in our favor is that through repeated diagnostic measurements we have shown that the Medusa LINAC produces repeatable results at the same axial location and same pulse width. To ensure we are getting the environment and dose we expect, we typically calibrate two PIN diodes and two PCDs behind the test object such that we obtain correction factors for each of the four diagnostic devices mounted in fixed positions. The correction factors differ slightly with axial position and pulse width, so we always obtain calibration factors for each test condition. These are used to correct slight differences in machine performance shot to shot at the same location (typical variation 1-2% or less) for all testing. Our measurements of prompt radiation induced conductivity in fiberglass are available in a previous report [6]. Dosimetry techniques and uncertainties at the Medusa LINAC are detailed in SAND report [7].

4. Analysis

A diagram of the measurement circuit for a single cell (either the URC or LRC) is shown in Figure 10. The dielectric samples are represented by a fixed capacitance C_s , which is the sum of the parallel capacitances of the two layers. R_{cell} is due to the dark conductivity, and R_{ric} is the variable radiation induced resistance. The direct drive current source across the sample, due to slight imbalances in the beam current in upper and lower dielectric regions of a cell, is labeled I_{dd} . This source is responsible for the current in the circuit when the cell is unbiased by either the external bias applied or any internal trapped charge bias.

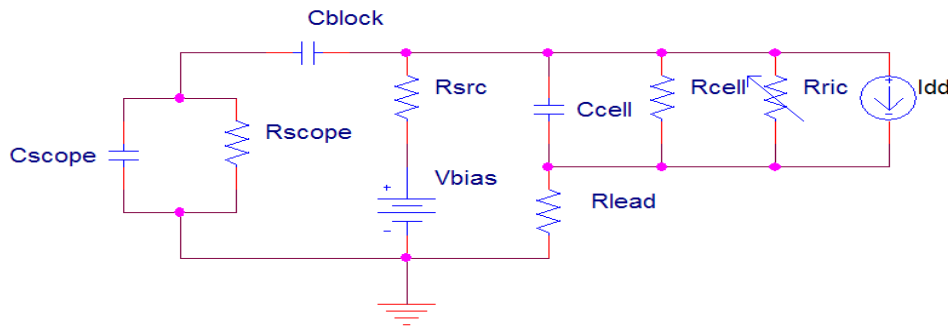


Figure 10 Equivalent Electrical Measurement Circuit

The blocking capacitor is selected so that the RC decay time is much greater than the radiation pulse width, so it can be considered a source of constant DC voltage V_C . The measured potential $V_R(t)$ across R_{scope} is used to determine the current through the

circuit. Abbreviating $V_{\text{bias}} = \mathbf{V}_B$, a loop rule gives $V_B = V_R + V_C$. Assuming the material is Ohmic, and denoting R_{scope} as \mathbf{R} , the current in the circuit is

$$I = \frac{V_C}{R_{\text{ric}}} + I_{dd} = -\frac{V_R}{R}. \quad (3)$$

Both linear and non-linear current characteristics have been found for RIC in insulators. For example, Yadlowsky and Hazelton [8] reported on the nonlinear steady-state current characteristic of Kapton H irradiated by 45 keV electrons. We can use (3) by absorbing all nonlinearity in the RIC conductivity \mathbf{R}_{ric} , for instance by allowing it to depend on the electric field. Using these two relations we can relate V_R to V_B :

$$V_R = \frac{V_B}{1 - \frac{R_{\text{ric}}}{R}} - \frac{R_{\text{ric}} I_{dd}}{1 - \frac{R_{\text{ric}}}{R}}. \quad (4)$$

If the RIC resistance is constant, it can be determined from the linear relationship between the bias voltage and the measured voltage in (4). The advantage of this is the direct drive component only appears in the constant term. The dose rate dependence of prompt RIC in amorphous solids (where the conductivity is from fast electrons) is often modeled as

$$\sigma_p = k_C \dot{D}^\Delta \quad (5)$$

Where \dot{D} is the dose rate, k_C is a constant RIC coefficient, and Δ is a parameter between 0.5 and 1. This makes the units of k_C the somewhat awkward $\text{mho}/(\text{rad/s})^\Delta$. Instead of assuming a power law, we can gain more flexibility by allowing the RIC coefficient k to depend on any of the experiment parameters, and taking $\Delta = 1$, so $\sigma_p = k(\dot{D}, D, E, \dots)\dot{D}$. It is this k , with units of $\text{mho}/(\text{rad/s})$, we refer to as the RIC coefficient.

Since the RIC cell is a triode configuration, there are two paths through dielectric layers from the center electrode to ground. The resistance through one branch can be written as

$$R_1 = \frac{d}{A\sigma_1} = \frac{d}{Ak\dot{D}_1} \quad (6)$$

with an identical relation for the second branch. The total resistance through the cell is

$$R_{\text{ric}} = \frac{R_1 R_2}{R_1 + R_2} = \frac{d}{Ak(\dot{D}_1 + \dot{D}_2)} = \frac{d}{2A\sigma} \quad (7)$$

where the effective conductance σ depends on the average dose rate in the two dielectric layers.

From (4), the conductance can be found from the slope m of V_B vs. V_R :

$$\sigma = -\frac{d}{2AR} \frac{m}{1-m} \quad (8)$$

If $m \ll 1$ then (8) becomes

$$\sigma \approx -\frac{dm}{2AR} \quad (9)$$

and the intercept in (4) becomes proportional to the scope resistance R :

$$V_R = mV_B + RI_{dd} \quad (10)$$

For a narrow range of dose rates, the conductivity should be nearly linear (k should be constant), and the RIC coefficient can be found from (7) and (10) as

$$k = \frac{1}{\dot{D}} \frac{d}{2AR} \frac{m}{m-1} \quad (11)$$

The only assumption is that $k(\dot{D})$ varies slowly enough to make the linear approximation (11) locally valid. Since the dose rate will vary from shot to shot, we can define $\mu = m/\dot{D}$ and (assuming $m \neq 1$) use

$$\frac{V_M}{\dot{D}} = \mu W_B + \frac{I_{dd}R}{\dot{D}} = \mu W_B + \beta \quad (12)$$

to determine the slope μ . The RIC coefficient k is then determined by

$$k = \frac{d}{2AR} \frac{\mu}{1 - \mu\dot{D}} \quad (13)$$

where we use the average dose rate for \dot{D} .

Dose Rates

Dose rates were determined with a combination of total dose data from TLD's and the electron beam waveform data from diamond PCD's. Using only the front collimator, dose measurements were taken with a TLD at the sample position and at the back window, where it would be located during the RIC shots. The ratio of the dose measurements in the RIC cell plane and at the back window, around a factor of two, is used scale the TLD measurements to the dose at the sample location.

We performed these measurements offsetting the entire apparatus at depths of 0", 2" and 4" from the front of the linear accelerator. Over this range, the measured dose decreases by a factor of three, showing significant beam divergence.

To relate the TLD dose measurements to the dose in the Kapton, we performed calculations using ADEPT and MCNP. The thinness of the samples and high energy of the electrons create some computational problems. The ONELD solutions are unstable with the default group structure. A logarithmic 100-group structure for electrons calmed these instabilities, but was still unable to reveal fine dose profiles.

Energy Deposition

The transport results for energy deposition are summarized below. The LiF TLD has a density of 2.635 g/cc, and the Si TLD has a density of 2.33 g/cc. Both have a thickness of 3 mil, or 0.00762 cm.

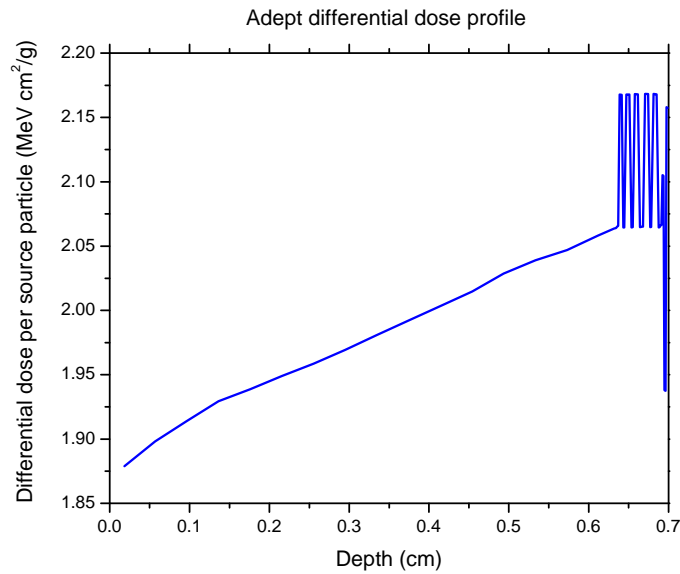


Figure 11 The differential dose profile computed by Adept.

The computed dose profile (figure 11) shows a steady dose enhancement effect. The first 0.63 cm is the aluminum scatter plate. The alternating layers of the RIC cells are seen at the far right. A comparison of the energy deposition computed by Adept and MCNP is shown below.

Energy deposition computed by MCNP and Adept

Layer	MCNP MeV/source	MCNP MeV cm ² /g	Adept Mev cm ² /g
URC 1	2.14E-2	1.98	2.17
URC 2	2.09E-2	1.93	2.17
LRC 1	2.16E-2	2.00	2.17
LRC 2	2.12E-2	1.96	2.17
LiF TLD	3.81E-1	1.62	1.95
Si TLD	3.69E-1	1.78	2.16

The important numbers for this study are the dose ratios between the TLD and the Kapton layers.

Computed Kapton to TLD dose ratios

Layer	LiF MCNP	LiF Adept	Si MCNP	Si Adept
URC 1	1.22	1.12	1.11	1.00
URC 2	1.19	1.12	1.08	1.00
LRC 1	1.23	1.12	1.12	1.00
LRC 2	1.21	1.12	1.10	1.00

The MCNP results are consistently about 10% higher than the Adept results. This means the computed dose in the Kapton will be lower, and the resulting RIC coefficients will be greater. We have chosen to use the MCNP results since (1) The ONELD results were exhibiting numerical instability, which may not have been fully eliminated, and (2) the MCNP results show more structure, for instance the extra dose enhancement seen in the LRC 1 layer, which is expected due to the double thickness of aluminum electrodes between the upper and lower cells. The Monte Carlo error in the MCNP results is no more than ± 2 in the last digit.

To further evaluate the accuracy of the dose computations, consider shot 2021 (from August 2005) for nominal values. The corrected dose in the LiF TLD is $2.84\text{E}+4$ rads. The MCNP result of $3.29\text{E}-1$ MeV per source particle deposited in the 35 mil thick TLD requires $2.14\text{E}+12$ electrons to reach the measured dose level. This implies a source current of 0.70 A over the measured $4.98\text{E}-7$ s pulse width. The reported approximate beam current is 1.6 A. However, the full beam area (estimated by radiochromic film) is 5.10 cm^2 , and only a 1.98 cm^2 collimated area enters the RIC cell and the TDL. If we scale the 0.70 A up to the full beam width, assuming a uniform current profile, the MCNP dose predicts a full beam current of 1.78 A, in reasonable agreement.

Charge Deposition

The simulation results for charge deposition are shown in the table below.

Computed charge deposition

Layer	MCNP charge deposition/e per source	MCNP electrons cm^2/g	Adept electrons/cm^2/g
URC top ground	+2.5E-3	-0.14	.0226
URC Kapton 1	-2.2E-3	0.12	.0203
URC center electrode	+3.2E-3	-0.18	.0218
URC Kapton 2	-2.0E-3	0.11	.0195
URC bottom ground	+9.6E-4	-.054	.0212
LRC top ground	+2.2E-3	-0.12	.0211
LRC Kapton 1	-2.4E-3	0.14	.0189
LRC center electrode	+3.1E-3	-0.17	.0208
LRC Kapton 2	-2.8E-3	0.15	.0188
LRC bottom ground	+1.5E-3	-0.084	.0209

The CEPXS charged particle deposition shows all positive numbers, representing negative charge deposition in each layer. The MCNP results show a net charge knock-off from the electrodes, and electron deposition in the Kapton.

Figure 12a shows a comparison of the source energy spectrum (blue) to the spectrum of forward electrons at the interface of the first URC Kapton layer (red), as computed by MCNP. It shows a large low energy component due to knock-on electrons entering the dielectric. The reverse electron spectrum at the end of the first URC layer shows low-energy back scatter from the center electrode (Figure 12b).

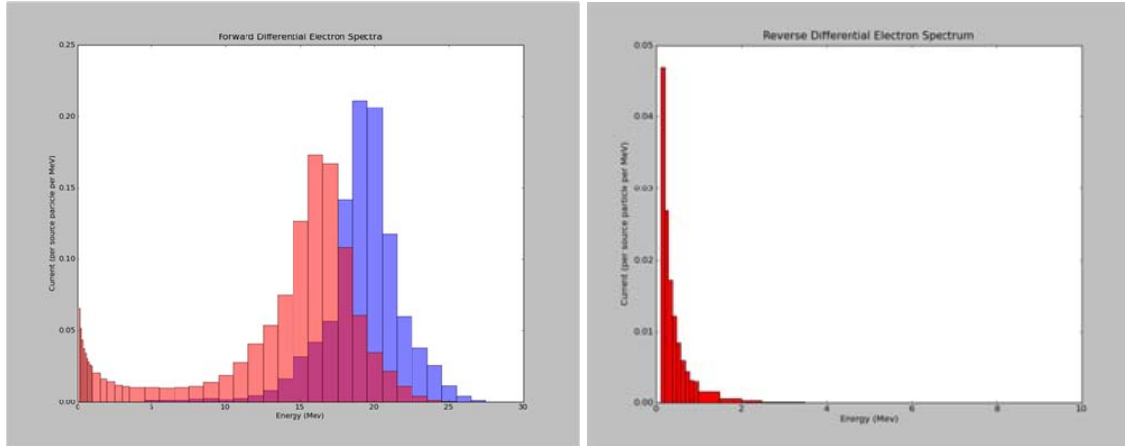


Figure 12 Electron energy spectra from MCNP.

12 (a) is a comparison of the source energy spectrum (blue) and the energy spectrum in the first Kapton layer. 12 (b) is the backward electron spectrum at the center electrode.

The secondary electrons flowing into the Kapton mostly have energies less than 2 MeV, and most commonly between 1 and 2 keV, which is the lower limit on the electron energies in MCNP. The number-weighted average energy of the reverse electrons is about 0.5 MeV. These electrons will also probably have a large angular spread, which will shorten their penetration into the dielectric.

MCNP shows that a large fraction of the electron deposition in the Kapton is within one micron of the electrodes. We were unable to get meaningful results from Adept over such small distances.

5. Results

A summary table of the test series is shown below. Each test series consisted of many shots with varying bias, with the same beam parameters. The average values of these parameters for each series of shots are given for reference.

Date	Kapton Sample	Series Designation	Mean Pulse FWHM (s)	Nominal dose rate (rad/s)
6/2005	1	K1	4.9E-7	6.5E10
6/2005	2	K2	5.1E-7	4.1E10
8/2005	3	K3a	5.0E-7	6.8E10
7/2007	3	K3b-1	4.9E-7	2.15E9
7/2007	3	K3b-2	4.9E-7	3.85E9
7/2007	3	K3b-3	5.0E-7	7.40E9
12/2008	3	K3c	3.8E-8	1.2E11

12/2008	5	K5	3.5E-8	1.2E11
---------	---	----	--------	--------

Data Reduction

The data is processed with baselining and smoothing. The raw data for the zero bias LRC signal of shot 1197 (July 2007) is shown in figure 13 below. There is a noise level of about 1 mV, as well as a few anomalous spikes. The entire dataset ranges over 5 μ s, and the pulse itself is contained within one μ s (the beam FWHM is 0.484 μ s). The sampling rate is 1.00 ns. The data after applying a 65-point second order (quadratic) Savitzky-Golay filter is shown on the right. This amounts to smoothing the signal over a 0.035 μ s window.

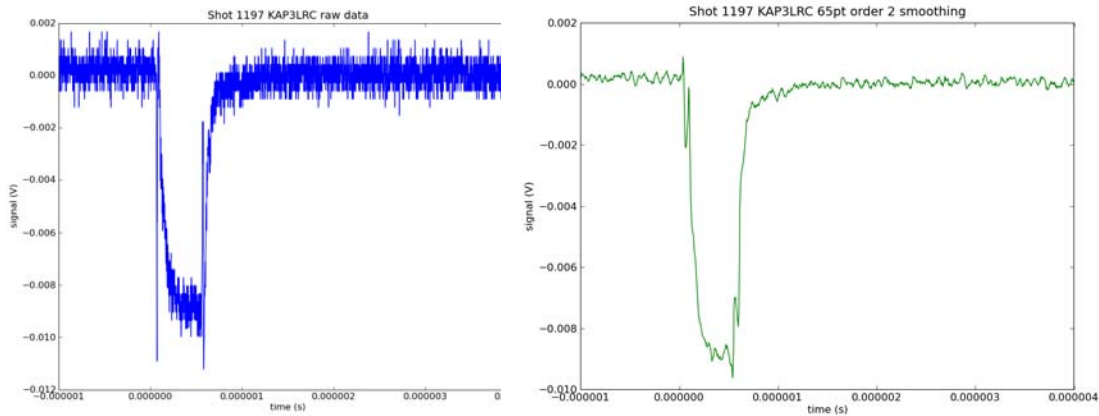


Figure 13 Shot 1197 data, raw and with a 65 point Savitzky-Golay filter applied.

This filter level barely suppresses the anomalous spikes, while maintaining features of the signal. Signals obtained from shots with bias suffer less from the effects of noise. For example, the raw data for shot 1188 at 600 V bias (from the same series) is shown in figure 14.

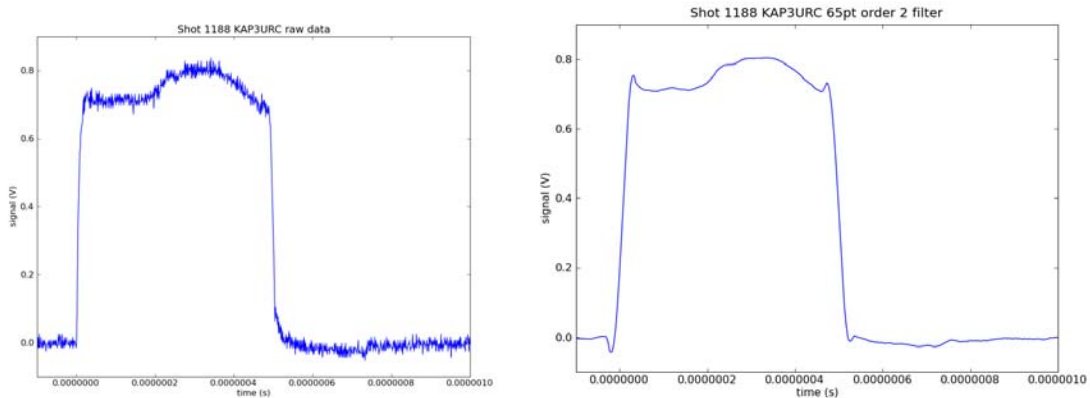


Figure 14 Raw and filtered data from shot 1188 (series K3b).

Direct drive measurements

The zero bias response is an indication of how much imbalance there is on the average electron current between the top and bottom Kapton regions of an individual cell. A typical zero-bias waveform from the K2 series is shown in Figure 15. In this and all subsequent figures, the PCD signal is rescaled to fit on the plot to show the shape of the beam waveform only. The URC signal is shown in red, and the LRC signal in blue. The peak signal values (in Volts) are printed beside the wave forms in the corresponding color.

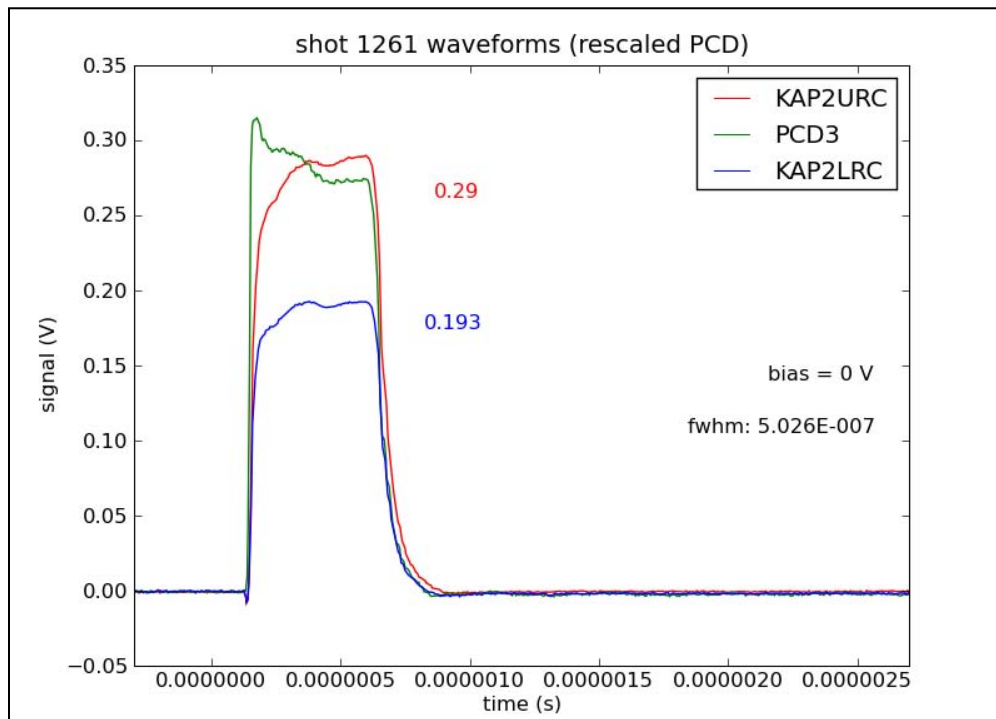


Figure 15 Typical zero bias waveforms.

The electron beam waveform, as recorded by the PCD, peaks early and plateaus. The zero-bias cell response has a short delay and gradually increases. It appears to be nearing a steady-state toward the end of the pulse, where it follows the decline with a short delay. The peak voltage of 0.29 V in the URC corresponds to a direct-drive current of 5.8 mA.

In the K3b series, we often see behavior in the URC signal that looks like a RIC signal with low voltage (Figure 16).

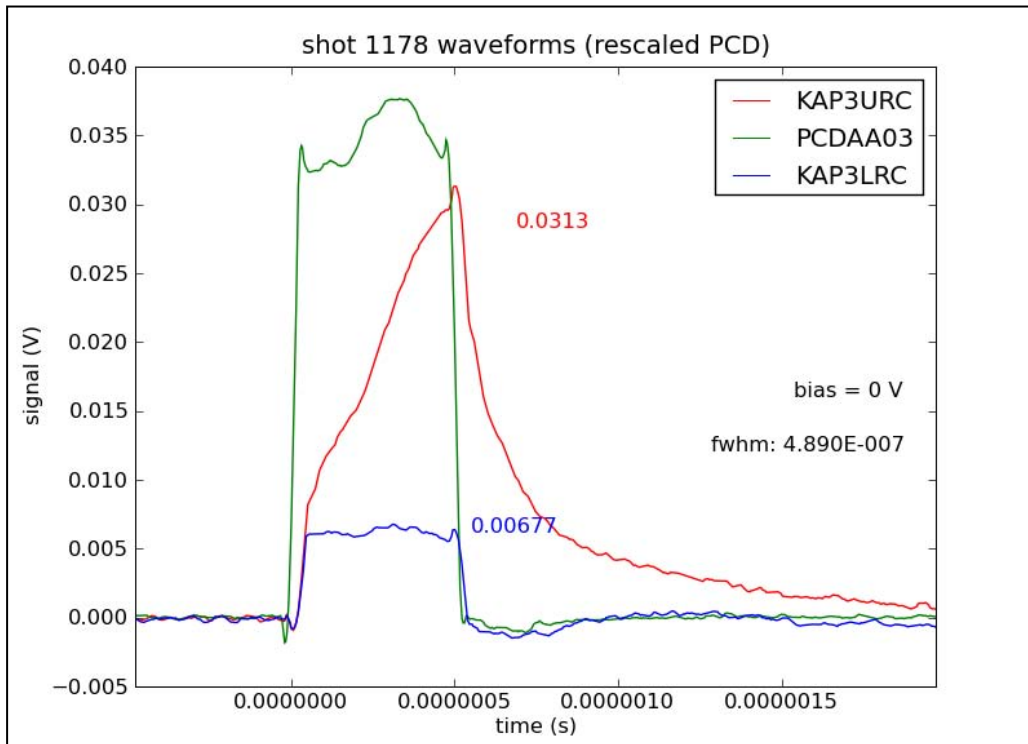


Figure 16 Zero bias shots from series K3b.

The nearly linear rise and post-pulse decay of the conductivity are typical features of biased shots. This is seen in most zero bias waveforms of the K3b series, but in no other series, indicating the URC was subject to a small bias during these shots.

A plot of the peak measured zero-bias voltage versus dose rate for the K2 series is shown in Figure 17.

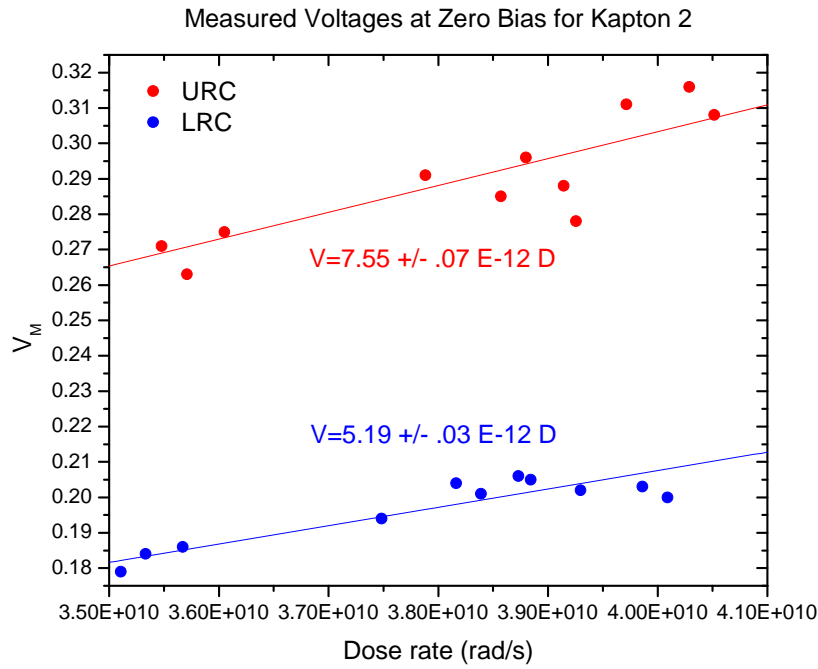


Figure 17 Peak measured voltage of zero bias shots vs. dose rate, with linear fits.

Assuming negligible lead resistance, the zero-bias current can be determined by

$$I_{dd} = \frac{V_M}{R} = \frac{\eta \dot{D}}{R} \quad (14)$$

where η is the slope of the zero bias plot. So we should have

$$\eta = \frac{RI_{dd}}{\dot{D}} = \beta \quad (15)$$

where β is the intercept from (12). Thus, we should be able to match the slope of zero bias shots vs. dose rate to the intercept of the V_M vs. V_B plot. This provides a check of the data quality.

Comparisons are shown in the table below.

Sample	eta	beta
K2 URC	7.55E-12	5.97E-12
K2 LRC	5.19E-12	5.83E-12

Considering the small signals in the zero bias shots, and their susceptibility to noise, the agreement is not bad.

Biased Response

A typical set of waveforms from a biased shot is shown in Figure 18. This shot is from the K3a series.

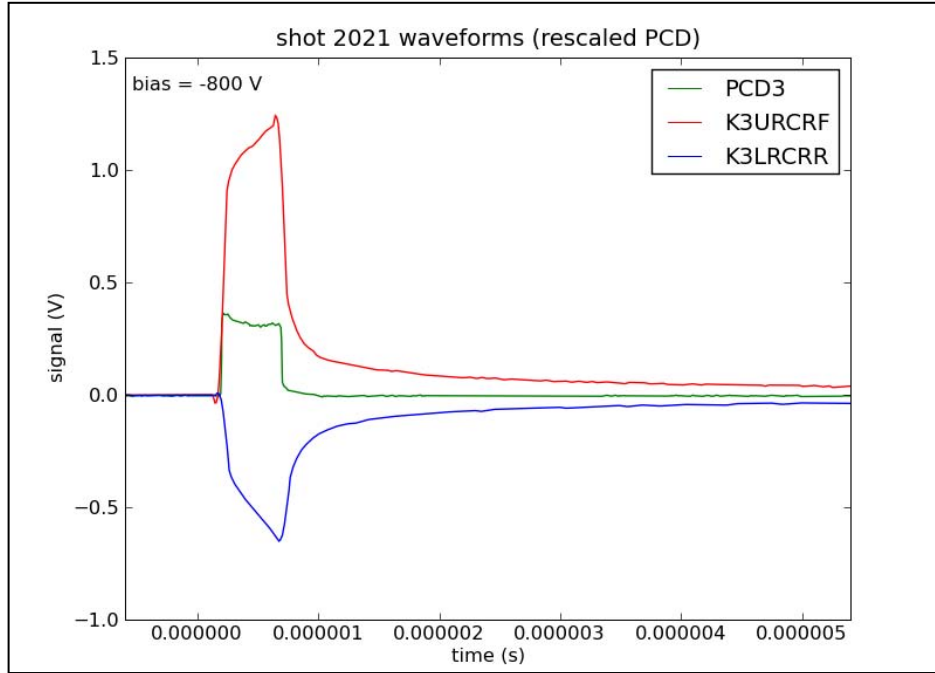


Figure 18 PCD and RIC signals for Shot 2021 of series K3a.

The PCD signal was scaled to have the same integral as the average of the other two. The PCD recorded a very flat electron beam wave form. The currents through the RIC cell initially rise with the pulse, but continue to increase almost linearly while the pulse is steady. In some series, the RIC signal does appear to approach a constant (similar to the zero bias signal shape), while in others like the above, the current does not appear to be saturating by the end of the pulse. The shape and size of the current buildup indicate it is much more than the rise observed in the direct drive component.

After the pulse, the cell current exhibits some delayed RIC, dissipating with a time constant around 40 ns. This is roughly an order of magnitude smaller than the pulse width, and should represent the time required for electrons to free themselves from shallow traps (since the carrier lifetime is generally estimated to be far shorter than this).

Weingart [9] reported a conductivity decay time of 90 ns, but this constant should vary with the applied field due to the Poole-Frenkel effect [10].

The buildup of the current observed in biased signals is probably caused by an increase in electron temperature due to collisions between conduction electrons and trapped electrons [11] [12]. Using this theory, Simpson [13] found a current equilibration time of 10^{-5} to 10^{-4} seconds for a soda-lime glass. However, this is hard to reconcile with the waveforms reported by Weingart [9], which show the conductivity rising exactly with a 40 ns x-ray

pulse. Since this pulse was smoothly varying (rather than resembling a square pulse), the rise in conductivity probably reflects the increasing population of conduction electrons from ionizations, rather than secondary effects. His charts also look hand-drawn, so may not be reliable.

A study of how this buildup varies with different pulse widths, and with different electric fields, should help reveal its physical nature. The latter is to some extent possible with the present data, but it would be preferable to use longer pulse widths to be able to directly view the equilibration time. This is beyond the scope of the current study.

The experiments conducted in December 2008 (series 3c and 5) used shorter pulse widths of around 35 ns. A typical biased waveform is shown in Figure 19. In this case, the width of the pulse is on the order of the relaxation time of the RIC, so the current does not approach equilibrium. The RIC signals seem to suffer from a short delay compared to the PCD signal. The measured conductivity of these shots is always less than the other series, since the RIC current has much less time to rise.

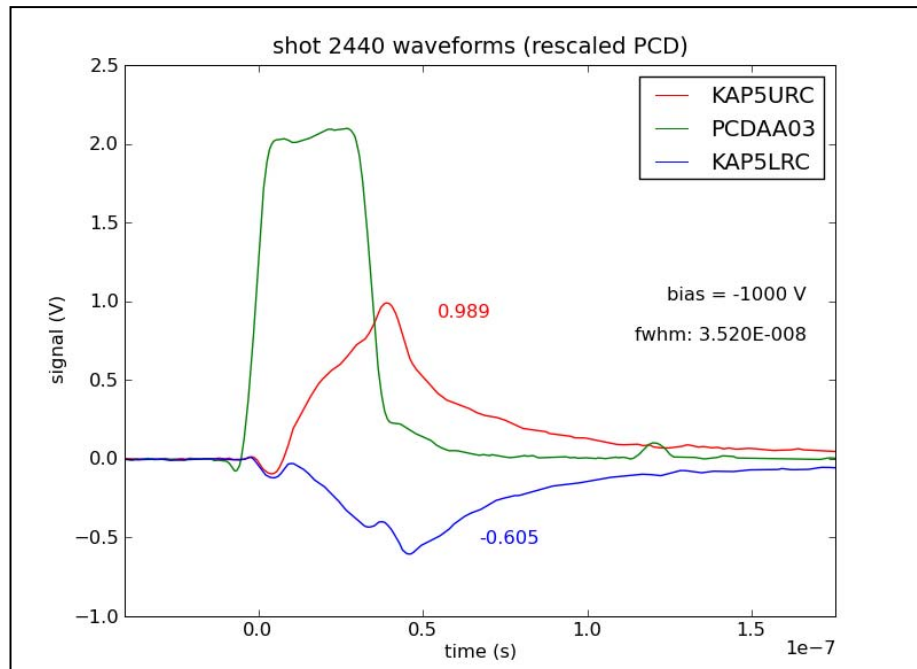


Figure 19 Shot 2440 from Series 3c.

In this signal, the LRC has positive bias, which should drive the RIC current opposite the direct drive current. Initially, the two nearly cancel, but the buildup of the RIC current is then seen as the signal voltage drops. When the pulse is over, the delayed RIC is driven by the bias. Note the initial dip of the RIC waveforms, and the upwards bump just before 50 ns. These features are also apparent in most other series (see Figures 17 and 19), but are especially prominent when the pulse width is short and the RIC is small. These features are always in the same direction for both signals, which have opposite bias. While these features might be brushed off as measurement artifacts, it's worth considering possible physical sources.

The MCNP simulations show a net electron loss from the electrodes to the surrounding Kapton layers. Those features may be from an initial current knocked off the aluminum electrodes, then discharged back onto the electrodes at the end of the pulse. This current would equilibrate as electric fields from local charge deposition and RIC drive a return current.

Using the above shot 2440 as an example, the TLD measured a dose of $3.86\text{E}+3$ rads(Si) over a FWHM of $3.54\text{E}-8$ s. MCNP records a dose of 0.369 MeV per source particle in the Si, implying $2.68\text{E}+11$ source particles, and a charge deposition of $1.25\text{E}-10$ Coulombs on the URC center electrode. This implies a nominal knock-off current of 2.7 mA. The features in figure 16 are about 0.1V, indicating a current of 2 mA.

In shot 2021 (figure 15), the dip goes to -0.04 V and has a width of about 45 ns. The corresponding bump has a height of 0.05 V and about the same width. This signifies a peak current of about 1 mA, whereas the calculation based on MCNP predicts a current of 1.8 mA.

Transport results agree well with the *size* of the features, but can they also explain the time scale? In shot 2440, supposing these electrons form a virtual cathode in the Kapton, the electric field will grow at a rate of $6.92\text{E}+14$ V/m/s (in one dimension, the strength of the field does not depend on where the cathode is located). MCNP indicates that most of the charge deposition occurs within one micron of the electrode. The dielectric breakdown of Kapton is about $1\text{E}8$ V/m. Based on the above rate, the field will reach this value in about $1.4\text{E}-7$ seconds. The features in figure 16 appear to be about ten nanoseconds. In the presence of RIC, the limiting field is probably considerably lower, and we do not have adequate information about the actual charge deposition profile. While the transport results support the hypothesis of charge knock-off and discharge to explain these features, there is too much physics unaccounted for to reach a solid conclusion.

This phenomenon is seen more clearly with low bias shots.

Two waveforms from series 5 are shown in figure 20. The first is a zero bias shot showing the direct drive current produced measured voltages of about 0.2. In the -500V bias shot, the LRC signal is actually initially driven slightly positive by the direct drive (after the initial knock-off dip). It is difficult to discern where the RIC buildup begins in the URC signal, but it is probably right around 0.2 V. It is only after the discharge bump around 40 ns that the LRC signal becomes significantly negative, *but this is only the delayed RIC*.

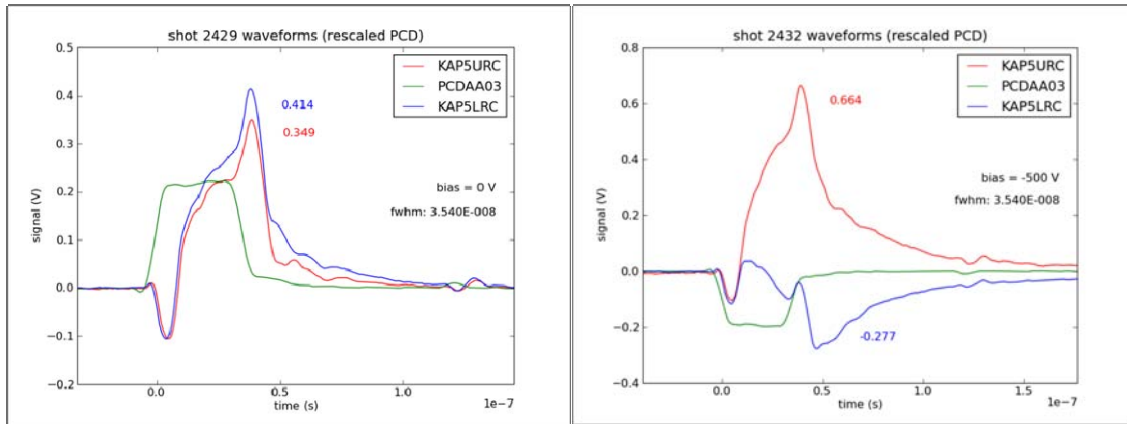


Figure 20 Shots from Series 5.

Previous studies [14] observed a discontinuity in the measured voltage vs. bias voltage plot. This is because, for the positive bias shots, they used the lowest measured voltage value. When the RIC is small, this is provided by the delayed RIC, which does not include the direct drive component.

For instance, the V_M / \dot{D} vs. V_b plot for K5 series is shown in Figure 21, where the positive and negative bias shots are fitted separately.

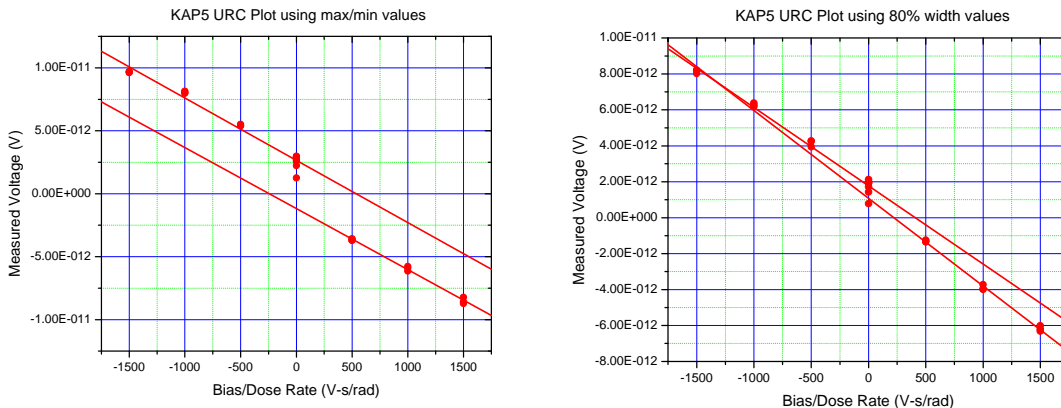


Figure 21 Comparison of RIC Coefficient fit for different methods of determining the peak voltage.

The first plot just takes the maximum signal value for negative bias shots and the minimum signal value for positive bias shots. The offset is due to the positive bias shots measuring the delayed RIC, where the effect of direct drive is removed. The second plot takes the value of the signals 90% of the way into the pulse (as determined by FWHM). Since this is during the pulse the direct drive component is present in both. This point was also chosen to try to avoid the discharge bump.

There is still a slight difference in slope. The positive bias shots consistently yield a slightly higher RIC conductivity. This is probably due to free electrons being attracted to the positively biased terminals. Most shots also included a background measurement, which was a text fixture with biased terminals, but no RIC cell. The background response for negatively biased cells is always negligible, but there is often a background response on positively charged terminals which is a significant fraction of the total response. This increases the signal in a way roughly proportional to the applied bias.

When there is a significant difference in slope, the negative bias data is used to determine the RIC coefficient. The negative bias data also aligns with the zero bias data, further indicating this is the correct data set to use. The intercept of the positive bias data is often slightly off, indicating there are additional physical effects present. This phenomenon becomes more pronounced with materials with a lower RIC coefficient than Kapton.

Previous studies [15] involving low dose rates and long exposure times (up to 7 hours) show that Kapton maintains a fairly steady value of conductivity for around 2E3 seconds (though it still seems to vary by up to 20% during this period, smoothly rising then falling), after which there is steep and steady increase in conductivity. While this study is not applicable to the regimes of this experiment, it illustrates there is no single RIC coefficient for the material, as it will depend on the dose history, dose rate, and applied voltage.

Determining the RIC coefficient

Figure 22 shows the data from the K2 series, plotting the measured voltage versus the bias voltage. The measured voltage is divided by the average dose rate for the series, for comparison with figure 23.

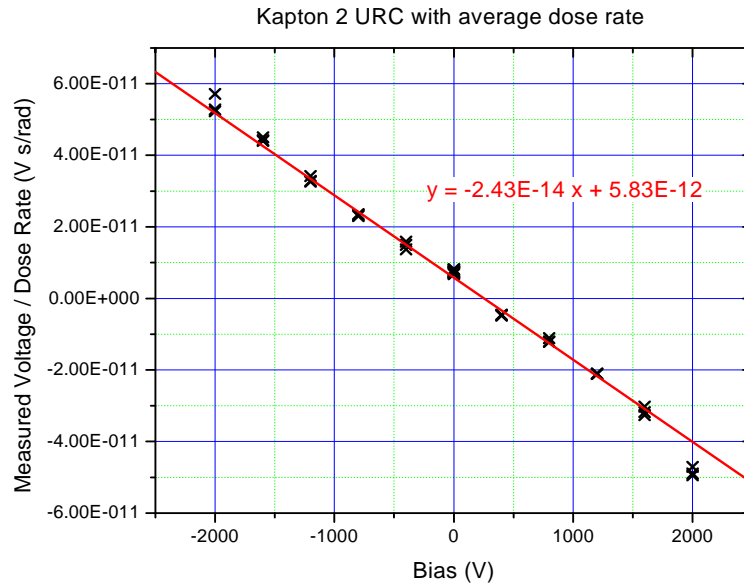


Figure 22 Determining the RIC coefficient for K2 URC using the average dose rate.

The same data, with the measured voltage of each point divided by the peak dose rate measured for each shot, is shown in figure 23.

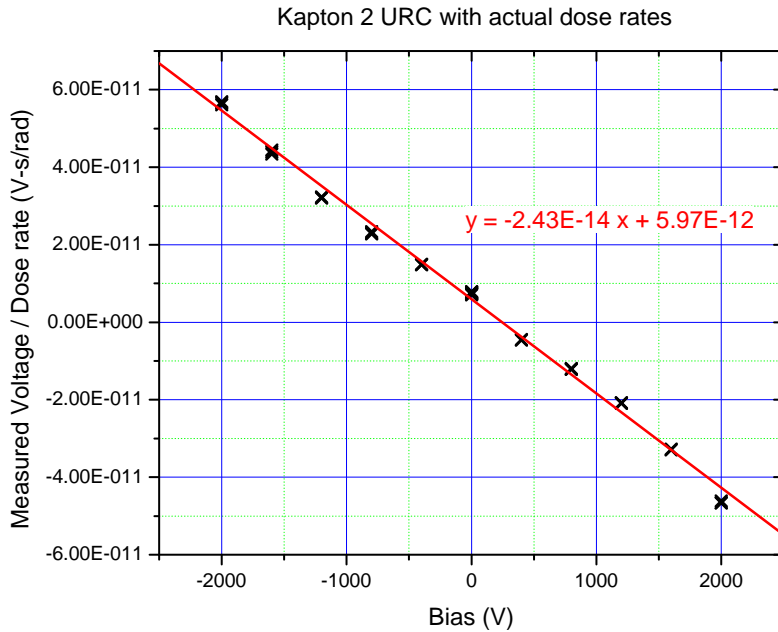


Figure 23 Determining the RIC coefficient of K2 URC using individual dose rates.

The vertical spread of the points has been reduced in figure 23. The fit of the slope to three figures has not changed, but the standard error of the fit has been slightly reduced. The symmetry of the plot suggests a slight nonlinearity. Simulations of the circuit with various parasitic elements have not produced this type of deviation. This may be due to nonlinearity of the current characteristic for RIC in the sample.

Summary

The results for each series are summarized below. All dose rates are rad(Kapton).

Series	Cell	Dose rate (rad/s)	K \square / (rad/s)	σ (\square)
K1	URC	6.5E10	6.6E-17	4.25E-6
K1	LRC	6.6E10	6.1E-17	4.0E-6
K2	URC	4.0E10	9.0E-17	3.6E-6
K2	LRC	4.1E10	8.3E-17	3.4E-6
K3a	URC	6.8E10	6.3E-17	4.3E-6
K3a	LRC	6.9E10	7.1E-17	4.8E-6
K3b-1	URC	2.4E9	1.1E-16	2.6E-7
K3b-1	LRC	2.4E9	9.5E-17	2.3E-7
K3b-2	URC	4.3E9	1.2E-16	5.1E-7
K3b-2	LRC	4.4E9	1.0E-16	4.4E-7
K3b-3	URC	8.2E9	1.3E-16	1.1E-6
K3b-3	LRC	8.3E9	1.1E-16	9.1E-7

K3c	URC	1.2E11	2.6E-17	3.2E-6
K3c	LRC	1.2E11	2.3E-17	2.9E-6
K5	URC	1.2E11	1.9E-17	2.3E-6
K5	LRC	1.2E11	2.1E-17	2.5E-6

Note again that the K3c and K5 series used a shorter pulse width than the rest, so must be compared separately.

The RIC coefficient for each shot series is plotted versus the average dose rate of the series in Figure 24. The sample/shot series are indicated by different symbols, while all of the URC and LRC cells are coded red and blue respectively. This plot assumes a conductivity linear in the dose rate, with a dose rate dependent coefficient. The downward slope indicates the conductivity is sub-linear with dose rate, so if using a power law model like (5), the exponent is less than one.

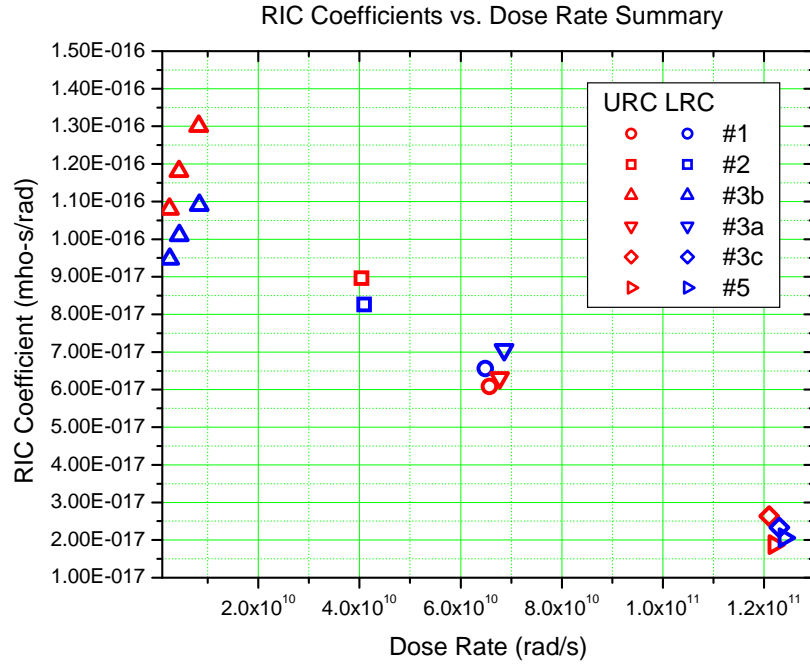


Figure 24 Summary of Measured RIC Coefficients.

Using the previous data to determine conductivity, its value versus dose rate seems to obey a law similar to(5), except for the 3c and 5 samples, which were performed with a smaller pulse width. The fit gives $k_c = 8.53E-14 \frac{\square}{m} \left(\frac{\text{rad}}{\text{s}} \right)^{-\Delta}$ with $\Delta = 0.713$.

This fit is shown in figure 25.

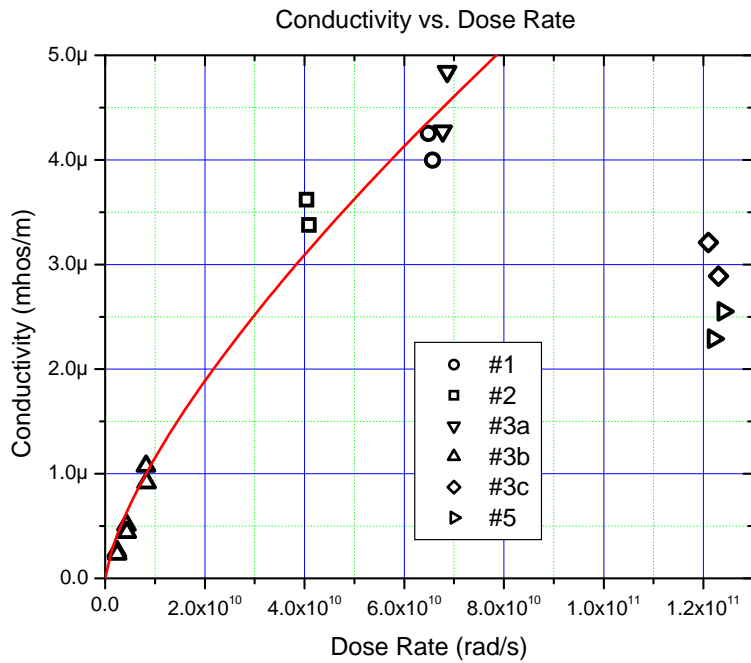


Figure 25 Summary of Conductivity Measurements with Fit (Excluding K3c and K5 series)

Comparisons

A summary of all the data on pulsed RIC in Kapton we are aware of is shown below.

Authors, date & Reference	Radiation type / facility	Nominal Energy	Pulse width or irradiation time	Dose rate
Weingart [16]	X-rays	10 keV	40 ns	1E9 to 1E10 rad(air)/s
Face [14]	X-rays: Kaman Febetron, AFRRI Linac, Boeing FX-75	500 MeV, ?, 3 MeV,	20, 200, and 35 ns	1E8 to 1E14 rad (LiF)/s
Present (2006-2008)	Medusa LINAC electron beam	20 MeV	500 ns	2E9 to 1E11 rad(kapton)/s
Present (2006-2008)	Medusa LINAC electron beam	20 MeV	35 ns	1E11 rad(kapton)/s

Comparisons of our data to previous results are shown in Figure 26.

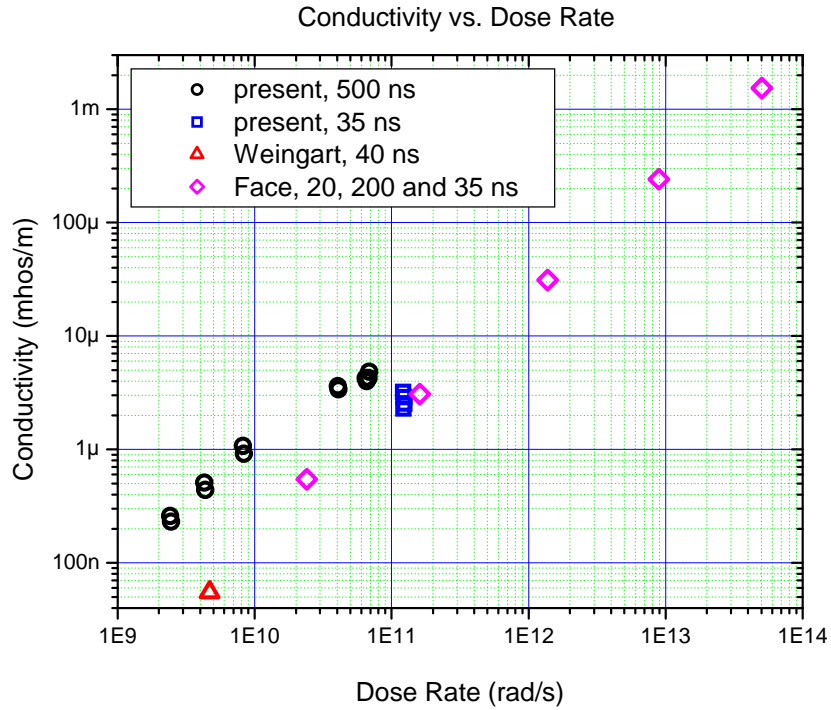


Figure 26 Comparisons of Conductivity with Previous Results.

Most of the previous measurements yielded significantly lower conductivities, but they also used shorter pulse widths. Weingart [9] used X-rays with a 40 ns pulse width, and Face [14] used several facilities with reported pulse widths of 20, 300, and 35 ns for low, medium, and high fluence results.

Bibliography

- [1] Thomas J. Ahrenst and Frederick Wooten, "Electrical Conductivity Induced in Insulators by Pulsed Radiation," *Nuclear Science, IEEE Transactions on*, vol. 23, pp. 1268-1272, 1976.
- [2] D. K. Nichols and V. A. J., "Theory of Transient Electrical Effects in Irradiated Insulators," *Nuclear Science, IEEE Transactions on*, vol. 13, pp. 119-126, 1966.
- [3] L. Weaver, J. Kenneth Shultis, and R. E. Faw, "Analytic solutions of a model for radiation-induced conductivity in insulators," *Journal of Applied Physics*, vol. 48, pp. 2762-2770, 1977.
- [4] J. F. Fowler, "X-Ray Induced Conductivity in Insulating Materials," *Proceedings of the Royal Society of London A*, vol. 236, pp. 464-480, 1956.
- [5] J. Mort and D. M. Pai, Eds., *Photoconductivity and Related Phenomena.*: Elsevier, 1976.
- [6] E. F. Hartman, "Measurements of Prompt Radiation Induced Conductivity of Fiberglass," Sandia National Laboratories Report SAND2010-2080 Sandia National Laboratories, 2010.
- [7] V. J. Harper-Slaboszewicz, "Dosimetry Experiments at the Medua Facility (Little Mountain)," Sandia National Laboratories Report SAND2010-6771 Sandia National Laboratories, 2010.
- [8] E.J. Yadlowsky and R.C. Hazelton, "Radiation induced conduction in Kapton H film," *Nuclear Science, IEEE Transactions on*, vol. 35, pp. 1050-1054, 1988.
- [9] R.H.; Hofer W.;; "Measurements of X-Ray-Induced Photoconductivity and Charge Transfers in Dielectric Structures," *IEEE Trans. Nucl. Sci. Vol. NS-19*, vol. 6, 1973.
- [10] J. Frenkel, "On Pre-Breakdown Phenomena in Insulators and Electronic Semiconductors," *Phys. Rev.*, vol. 54, pp. 647-648, 1938.
- [11] H. Fröhlich, "On the Theory of Dielectric Breakdown in Solids," *Proceedings of the Royal Society of London. Series A. Mathematical and Physical Sciences*, vol. 188, pp. 521-532, 1947.
- [12] H Fröhlich and J O'Dwyer, "Time Dependence of Electronic Processes in Dielectrics," *Proceedings of the Physical Society. Section A*, vol. 63, p. 81, 1950.
- [13] J H Simpson, "The Time Delay in Conduction and Breakdown Processes in Amorphous Solids," *Proceedings of the Physical Society. Section A*, vol. 63, p. 86, 1950.
- [14] Steven H. Face, Charles A. Eklund, and Thomas A. Stringer, "Measurement of Radiation Induced Conductivity for Hardened Cable Dielectric Materials at High Fluence," *Nuclear Science, IEEE Transactions on*, vol. 30, pp. 4450-4456, 1983.
- [15] R. Gregorio Filho, B. Gross, and R. M. Faria, "Induced Conductivity of Mylar and Kapton Irradiated by X-Rays," *Electrical Insulation, IEEE Transactions on*, vol. EI-21, pp. 431-436, 1986.
- [16] R. C. Weingart, R. H. Barlett, R. S. Lee, and W. Hofer, "X-Ray-Induced Photoconductivity in Dielectric Films," *Nuclear Science, IEEE Transactions on*, vol.

- 19, pp. 15-22, 1972.
- [17] V. A. J., J. W. Harrity, and T. M. Flanagan, "Scaling Laws for Ionization Effects in Insulators," *Nuclear Science, IEEE Transactions on*, vol. 15, pp. 194-204, 1968.
- [18] Berger and Seltzer, "Tables of Energy Loss and Ranges of Electrons and Positrons," NASA, 1964.
- [19] A.R. Frederickson, "Radiation Induced Currents and Conductivity in Dielectrics," *IEEE Trans. on Nuc. Sci.*, vol. #NS-24#, 1977.
- [20] A.R. Frederickson, S. Woolf, and J.C. Garth, "Model for space charge evolution and dose in irradiated insulators at high electric fields," *Nuclear Science, IEEE Transactions on*, vol. 40, pp. 1393-1401, 1993.

Distribution

1 MS 0447	J. F. Nagel, Jr.	2127
1 MS 0453	M. A. Rosenthal	2130
1 MS 1083	M. R. Shaneyfelt	17311
1 MS 1145	P. S. Raglin	1380
1 MS 1146	P. J. Griffin	1384
1 MS 1146	D. B. King	1384
1 MS 1152	C. D. Turner	1653
1 MS 1152	M. Caldwell	1653
1 MS 1152	M. F. Pasik	1654
1 MS 1152	B. D. Seidel	1654
1 MS 1159	C. E. Hembree	1344
1 MS 1167	T. A. Zarick	1343
1 MS 1167	M. L. McLain	1343
1 MS 1167	T. J. Sheridan	1343
2 MS 1167	E. F. Hartman	1343
1 MS 1179	M. A. Hedemann	1340
1 MS 1179	W. C. Fan	1341
1 MS 1179	H. P. Hjalmarson	1341
1 MS 1179	C. R. Drumm	1341
1 MS 1179	L. Lorence	1341
1 MS 1219	D. E. Beutler	5923
1 MS 1219	V. K. Hernandez	5923
1 MS 9106	C. L. Turner	8226
1 MS 9106	D. L. Gehmlich	8226
1 MS 9154	R. E. Oetken	8244
1 MS 9154	S. E. Faas	8244
1 MS 0899	Technical Library	9536 (electronic copy)

1 T. A. Stringer
 ITT Advanced Engineering & Sciences
 5009 Centennial Blvd. Colorado
 Springs, CO 80919

1 E. Preston
 ITT Advanced Engineering & Sciences
 5009 Centennial Blvd. Colorado
 Springs, CO 80919

